Supplementary Information (SI) for Inorganic Chemistry Frontiers.
This journal is © the Partner Organisations 2024

Supplementary information

Microwave-assisted fabrication of self-supported graphene-based high-entropy alloy electrode for efficient and stable electrocatalytic nitrate reduction to ammonia

Yun Ling,*[a,b] Qingyun Feng,[a] Xuan Zheng,*[a] Hui Su,[a] Yuanyuan Zhang,[a] Zehua Zou,[a] Aifen Liu,[a] Yang Huang, [a] Jing Tang,[c] Yi Li,[c] Maosheng Zhang[a] and Qingxiang Wang[a]

[a] *Fujian Provincial Key Laboratory of Modern Analytical Science and Separation Technology, Fujian Provincial Key Laboratory of Pollution Monitoring and Control, College of Chemistry, Chemical Engineering and Environment, Minnan Normal University, Zhangzhou 363000, China*

[b]*Key Laboratory of Advanced Energy Materials Chemistry (Ministry of Education), Nankai University, Tianjin 300071, China*

[c]*Key laboratory for analytical science of food safety and biology, Ministry of Education, College of Chemistry, Fuzhou University, Fuzhou 350116, China*

E-mail: lingyun@mnnu.edu.cn; zx1974@mnnu.edu.cn

Experimental sections

Chemicals and reagents

Ammonium chloride (NH_4Cl, ≥99.5%), sodium salicylate ($C_7H_5NaO_3$, ≥99.5%), trisodium citrate dihydrate ($C_6H_5Na_3O_7·2H_2O$, ≥99.0%), sodium hydroxide (NaOH, ≥96.0%), ferric chloride hexahydrate ($FeCl_3·6H_2O$, ≥99.0%), cobalt chloride hexahydrate ($CoCl_2·6H_2O$, ≥99.0%), nickel chloride hexahydrate ($NiCl_2·6H_2O$, ≥98.0%), copper chloride dihydrate ($CuCl_2·2H_2O$, ≥99.0%), stannous chloride dihydrate ($SnCl_2·2H_2O$, ≥98.0%), phosphoric acid (H_3PO_4, ≥85.0%), hydrochloric acid (HCl), sulfuric acid (H_2SO_4), sulfamic acid (NH_2SO_3H, ≥99.5%) and sodium

hypochlorite solution (NaClO, available chlorine 8.0%) were purchased from Xilong Scientific Co., Ltd. Ethyl alcohol (C_2H_5OH, ≥99.7%), sodium sulfate (Na_2SO_4, ≥99.0%), sodium nitroferricyanide (III.) ($C_5FeN_6Na_2O \cdot 2H_2O$, 99.0%), N-(1-Naphthyl)ethylenediamine dihydrochloride ($C_{12}H_{16}Cl_2N_2$, ≥97.0%) and aminobenzene sulfonamide ($C_6H_8N_2O_2S$, ≥99.8%) were purchased from Sinopharm Chemical Reagent Co., Ltd. Hydrophilic carbon paper (Taiwan CeTech Co., Ltd). Ar gas (99.999%) was purchased from Zhangzhou Xinxing Gas Co., Ltd.

Electrochemical tests

All electrochemical experiments were conducted in a Nafion 115 membrane-separated H-type electrolytic cell. A three-electrode system was employed, with the FeCoNiCuSn HEA catalyst as the working electrode, a platinum mesh as the counter electrode, and an Ag/AgCl electrode (filled with saturated KCl solution) as the reference electrode. The electrolyte used was 100 ppm NO_3^--N + 0.1M Na_2SO_4 solution (30 mL). Electrochemical measurements were performed using a DH7000 electrochemical workstation (Donghua Analytical, China). Linear sweep voltammetry (LSV) was conducted at a scan rate of 5 mV/s, within the potential range from 0 V to -1.1 V vs. RHE. Chronoamperometry tests were performed for 1 hour at -0.7, -0.8, -0.9, -1.0, and -1.1 V vs. RHE, respectively. The double-layer capacitance was obtained through cyclic voltammetry (CV) at different sweep rates (40, 60, 80, 100, 120, 140 and 160 mV s^{-1}) within the potential range of 0.1-0.3 V vs. RHE. Unless otherwise specified, the electrochemical optimization experiments were conducted at a potential of -1.0 V vs. RHE.

Characterization

Powder X-ray diffraction (XRD) patterns were obtained using a Rigaku-Ultima IV diffractometer with Cu Kα radiation (λ = 1.5406 Å). Scanning electron microscopy (SEM) and Energy Dispersive X-ray (EDX) mapping were performed using a GeminiSEM 300 high-resolution scanning electron

microscope. Transmission electron microscopy (TEM) and high-resolution TEM (HRTEM) were conducted with an FEI Tecnai G2 F30 microscope operating at 300 kV. X-ray photoelectron spectroscopy (XPS) spectra were collected using a Thermo Escalab 250Xi spectrometer. Raman spectra were acquired on a Nanophoton Raman-11 instrument with 532 nm laser excitation. Fourier-transform infrared (FT-IR) spectra were measured using a Nicolet iS10 spectrometer. Absorbance spectra were obtained using a Shimadzu UV-2600i UV-vis spectrophotometer. Microwave heating was carried out using an EMA34GTQ-SS microwave oven (Midea, China). The metal contents in the FeCoNiCuSn HEA catalysts were determined using an Agilent 5110-based ICP-OES.

Determination of NO_3^--N

First, a specific volume of electrolyte is extracted from the electrolytic cell and diluted to 5 mL to bring it within the detection range. Subsequently, 100 μL of 1 M HCl and 10 μL of 0.8 wt% sulfamic acid solution are added to the diluted sample solution. Following a 15-minute incubation period, the solution's absorbance is measured using a UV-Vis spectrophotometer at wavelengths of 220 nm and 275 nm. The final absorbance of NO_3^--N is calculated using the formula: $A = A_{220\,nm} - 2A_{275\,nm}$. This calculation corrects for any interference from other substances at 275 nm. To construct calibration curves, the absorbance of standard solutions of $NaNO_3$ at different concentrations is measured.

Detection of NO_2^--N

A mixture comprising of p-aminobenzenesulfonamide (4 g), N-(1-naphthyl)ethylenediamine dihydrochloride (0.2 g), ultra-pure water (50 mL) and phosphoric acid (10 mL) served as the color developing agent. Subsequently, a specific volume of electrolyte was extracted from the cell and diluted to 5 mL to ensure compatibility with the detection range. Next, 100 μL of the color developing reagent were added to the 5 mL solution and thoroughly mixed. After allowing the mixture to stand for 30 minutes, the absorption intensity at a wavelength of 540 nm was recorded.

Calibration curves were generated by measuring the absorbance of $NaNO_2$ solutions of various concentrations. These curves facilitated the quantification of the desired analyte based on its absorbance.

Determination of NH_3

The concentration of NH_3 was determined using indophenol blue spectrophotometry, following dilution of the resulting electrolyte. Specifically, 4 mL of the diluted electrolyte were mixed with 500 μL of developer A (containing 5 wt% $C_7H_5O_3Na$, 5 wt% $C_6H_5Na_3O_7$, and NaOH). To this mixture, 50 μL of developer B (0.05 M NaClO solution) and 50 μL of developer C (1 wt% $Na_2Fe(CN)_5NO{\cdot}2H_2O$ solution) were added. After thorough mixing, the absorbance was measured using UV-Vis spectrophotometry at a wavelength of 670 nm following a 1-hour incubation period. Calibration curves were established by measuring the absorbance of NH_4Cl solutions of varying concentrations.

Isotope labeling experiment

An isotopically labeled nitrate reduction experiment was conducted to confirm the ammonia source, using $Na^{15}NO_3$ (abundance: 99 atom%, chemical purity: ⩾98.5%) as the feed nitrogen (N) source. In this experiment, 0.1M Na_2SO_4 served as the electrolyte, and $Na^{15}NO_3$ with a concentration of 100 ppm $^{15}NO_3^-$-N was introduced as the reactant. The resulting $^{15}NH_4^+$-^{15}N electrolyte obtained through electroreduction was adjusted to pH=2 using 1 M H_2SO_4 and characterized by ^1H NMR with maleic acid as an external standard. To establish a calibration curve, solutions of $^{14}NH_4^+$-^{14}N standard ($^{14}NH_4Cl$ with concentrations ranging from 20 to 200 ppm) were prepared using 0.1 M Na_2SO_4 as the solvent. Subsequently, 50 mL of each concentration of $^{14}NH_4^+$-^{14}N standard solution was mixed with 1 mL of 20 mg mL^{-1} maleic acid. A 0.5 mL aliquot of the resulting mixture was combined with 90 μL of deuterium oxide (D_2O) for ^1H NMR detection. The concentration of

$^{14}NH_4^+$-^{14}N was determined by the area ratio, where the peak area ratio of $^{14}NH_4^+$-^{14}N to maleic acid was utilized for calibration purposes.

Calculation of yield, selectivity and Faradaic efficiency

The ammonia yield rate and Faradaic efficiency were determined using the following equation:

$$NH_{3\ yield} = (c_{NH_3} \times V) / (t \times S) \quad (1)$$

$$FE\ (\%) = (8 \times c_{NH_3} \times V \times F) / (17 \times Q) \times 100\% \quad (2)$$

The selectivity of ammonia and nitrite using were determined using the following equation:

$$NH_3\ selectivity\ \left(S_{NH_3}\right) = C_{NH_3}/\Delta C_{NO_3^-} \times 100\% \quad (3)$$

$$NO_2^-\ selectivity\ \left(S_{NO_2^-}\right) = C_{NO_2^-}/\Delta C_{NO_3^-} \times 100\% \quad (4)$$

where, c_{NH_3} is the measured NH_3 concentration, $c_{NO_2^-}$ is the measured NO_2^- concentration, V is the volume of the electrolyte, t is the NRA test time, S is the geometric area of the working electrode (1×1 cm^2), $\Delta c_{NO_3^-}$ is the concentration difference of NO_3^- before and after electrolysis, F is the Faradaic constant (96485 C mol^{-1}) and Q is the total charge used by the electrodes.

Computational Details

All spin polarization density functional theory calculations were performed by employing the Vienna Ab-initio Simulation Package (VASP).[1,2] The Perdew-Burke-Ernzerhof (PBE) functional within the generalized gradient approximation (GGA) was employed to evaluate electron exchange and correlation, while projector augmented wave (PAW) pseudopotential in conjunction with plane-wave basis set of 400 eV cutoff energy were used to describe the wavefunctions of system. [3, 4] To better consider the weak interactions between high entropy alloy (HEA) surface and NRA intermediates, DFT-D3 correction method was also applied.[5] Due to the computational complexity associated with exploring all configurations of FeCoNiCuSn HEA across the entire structural space, the Alloy Theory Automation Kit (ATAT) software was first employed to produce a FeCoNiCuSn

HEA model consisting of 80 metal atoms ($Fe_{12}Co_{20}Ni_{16}Cu_{24}Sn_8$) and 15 Å vacuum layer along the Z-axis.[6,7] Based on this HEA model, a set of HEA-NRA intermediate complexes were then established and undergone the structural optimization, and the atomic coordinates were collected until reaching the SCF energy and force convergence criteria of 1.0×10^{-6} eV and 0.05 eV /Å, respectively. During the structural optimization, the bottom two atomic layers of these models were fixed, and the Gamma-centered (3×3×1) k-point sampling was applied in the Brillouin zone for all calculations. The Gibbs free energy change of each NRA step was calculated by using the following equation:

$$\Delta G = \Delta E + \Delta E_{Z\ P} - {}_{E}T\ \ \Delta + Sn\ \ e\ \ U \quad (5)$$

Where ΔE and ΔE_{ZPE} represent the total electron energy difference and zero-point energy correction for each NRA step, respectively, while TΔS denotes the entropy correction at room temperature (298.15 K). n is the number of transferred electrons, U is the applied potential and is set as zero. To evade the inaccuracy of density functional theory (DFT) in calculating the energy of charged NO_3^- ions, gas-phase nitric acid molecule was adopted as a reference and a compensation correction value of 0.75 eV was applied to compute the $\Delta G_{N\ \ 3}$ by using equation 6.[8] As for the calculations of H_2, H_2O, and NH_3, a 15×15×15 Å^3 unit cell and only Gamma k-point were employed. Their ZPE correction were determined through vibration analysis, while the entropy values of these molecules (TS 0.40, 0.21, and 0.60 eV, respectively) were extracted from the standard thermodynamic table.

$$\Delta G_{N\ \ 3} = \Delta E_{(*N\ \ 3)} + \frac{1}{2}E_{(H_2)} - E_{(*)} - E_{(HN\ \ 3)} + 0\ \ .\ \ eV\ 5 \quad (6)$$

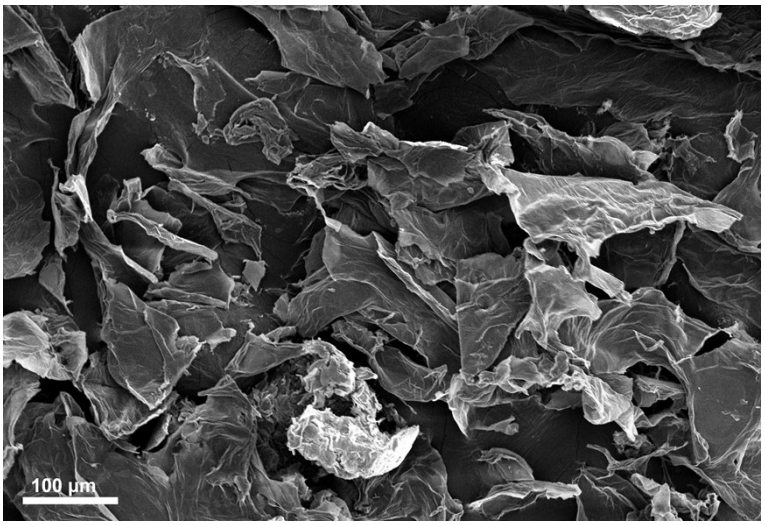

Fig. S1 The SEM image of GO.

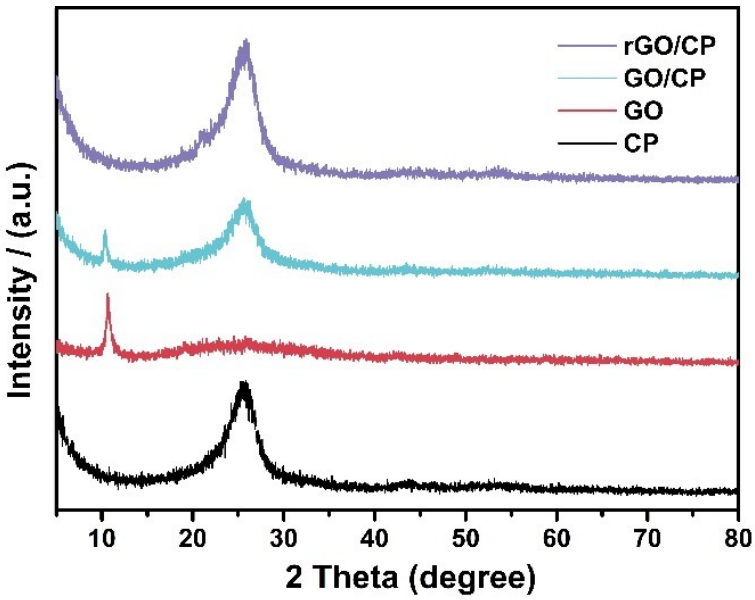

Fig. S2 XRD patterns of carbon paper (CP), GO, GO/CP and rGO/CP.

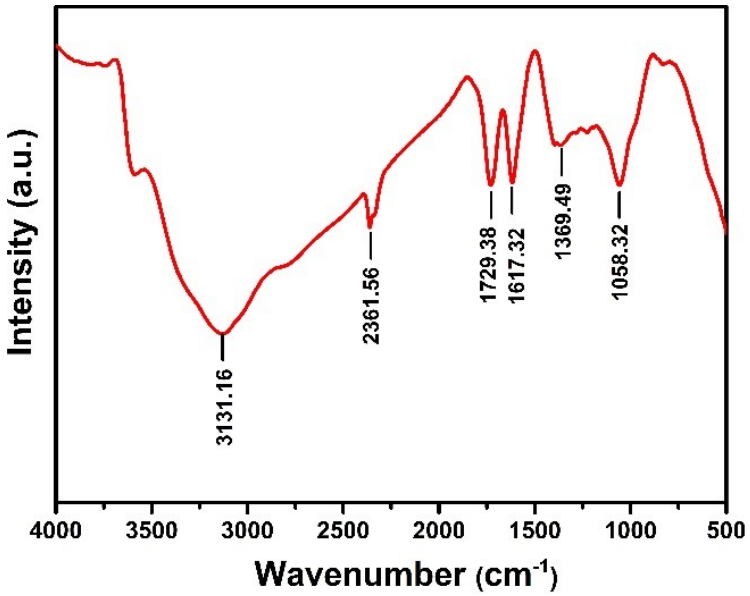

Fig. S3 FTIR spectra of GO.

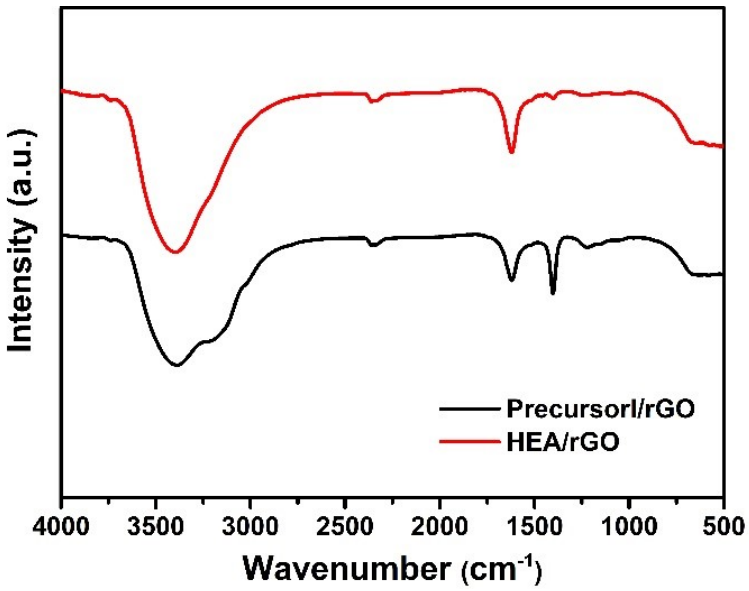

Fig. S4 FTIR spectra of precursorl/rGO and HEA/rGO.

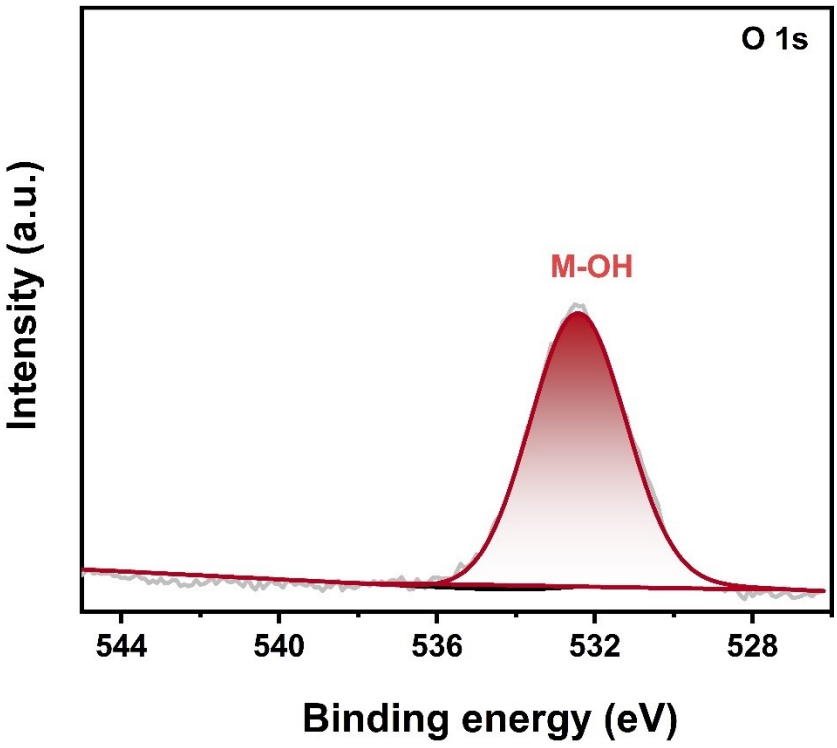

Fig. S5 O 1s of FeCoNiCuSn HEA.

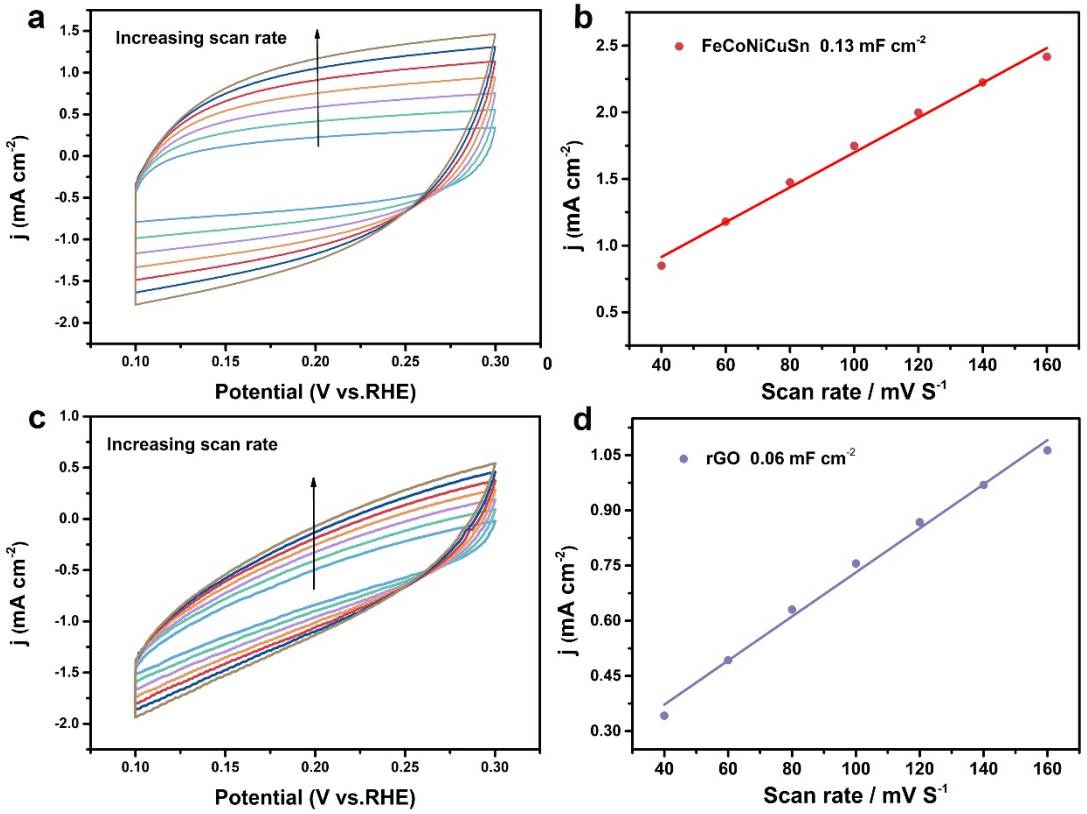

Fig. S6 Cyclic voltammetry measurements with various sweep rates (40, 60, 80, 100, 120, 140 and 160 mV s^{-1}) for HEA/rGO/CP (a) and rGO/CP (c). The corresponding double-layer charging current vs the scan rate, and the slope of the linear fit is double-layer capacitance (b, d).

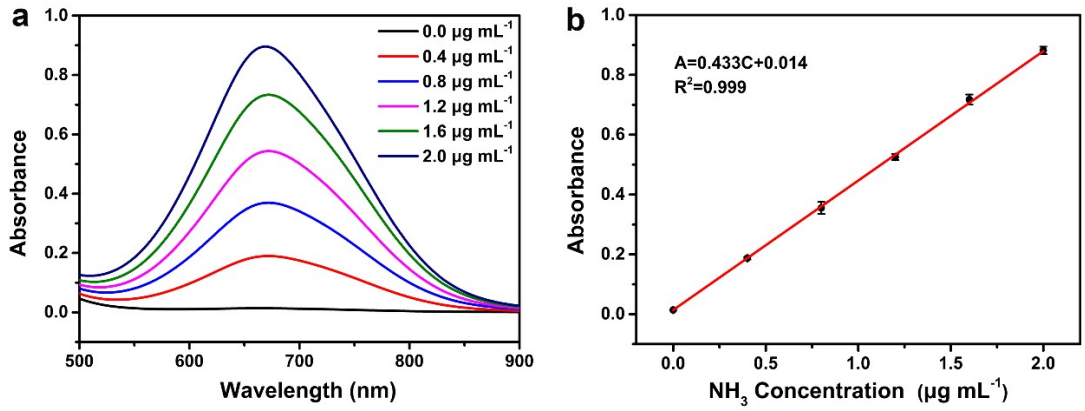

Fig. S7 (a) UV-Vis absorption spectra and (b) corresponding calibration curve used for calculation of NH_3 concentration.

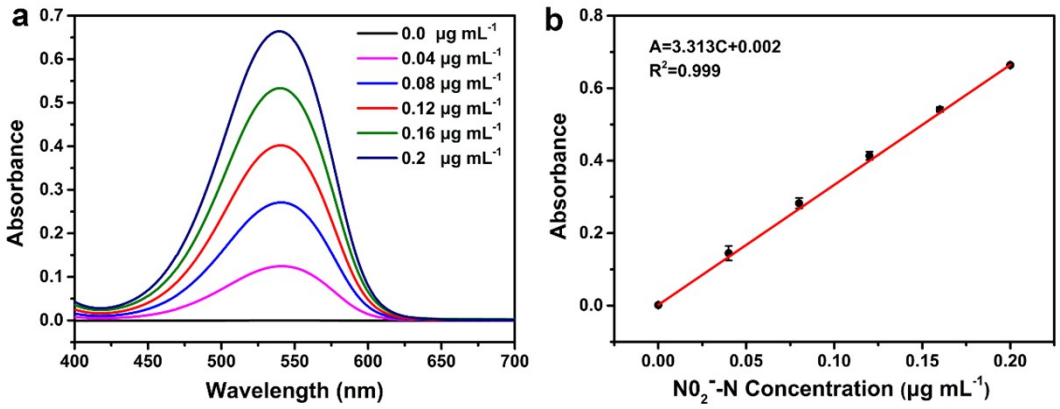

Fig. S8 (a) UV-vis absorption spectra and (b) corresponding calibration curve used for calculation of NO_2^--N concentration.

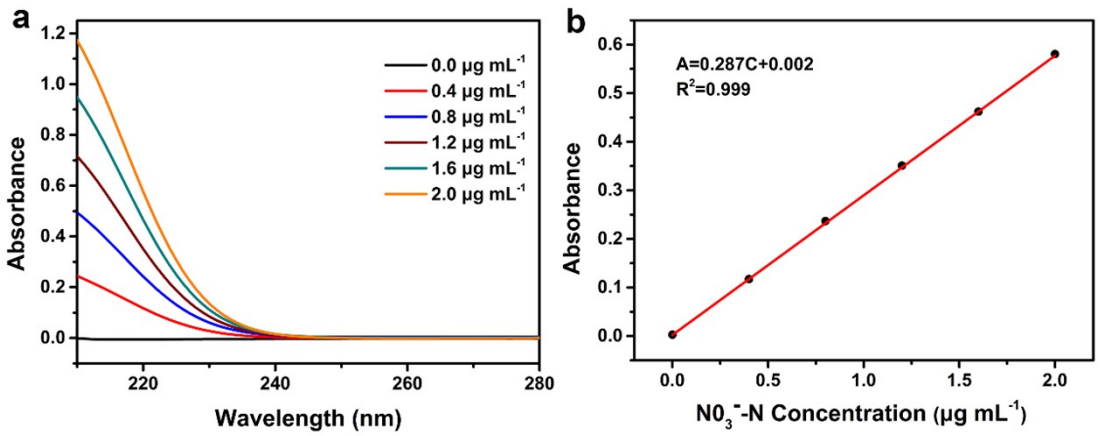

Fig. S9 (a) UV-vis absorption spectra and (b) corresponding calibration curve used for calculation of NO_3^--N concentration.

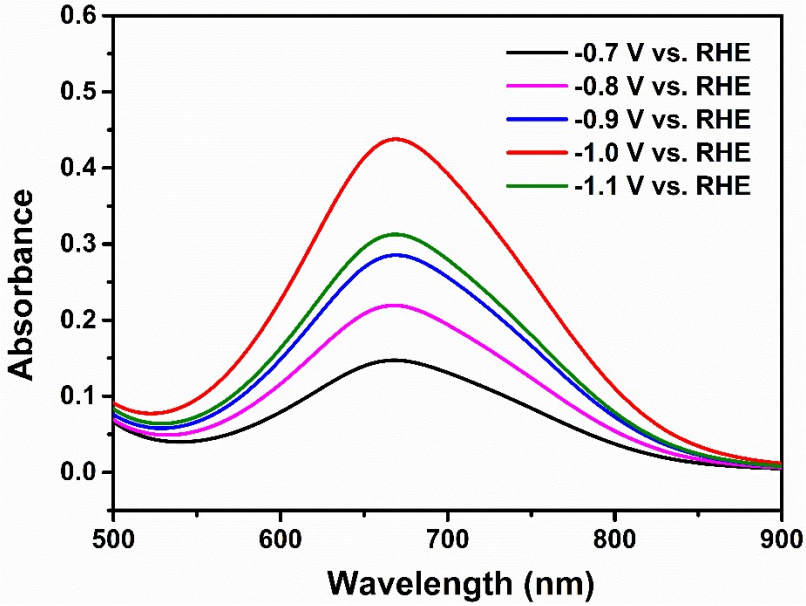

Fig. S10 UV–vis absorption spectra at different potentials.

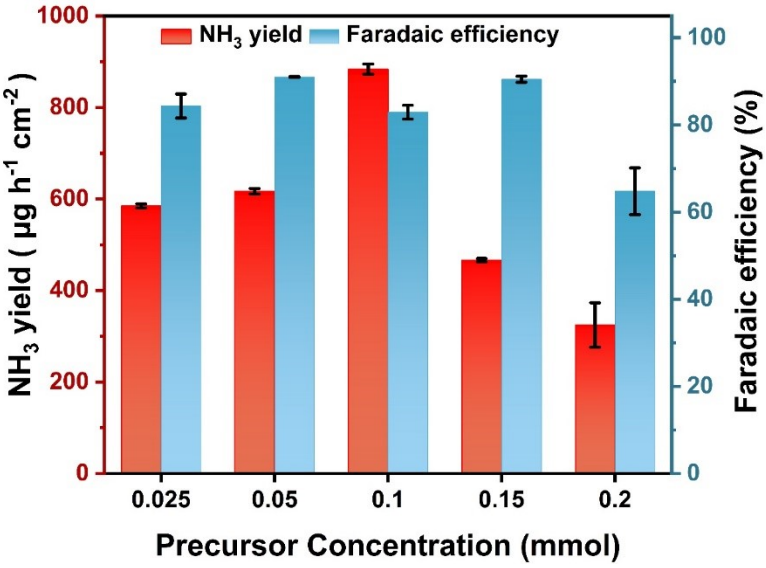

Fig. S11 NH_3 yields and FE with different precursor concentration.

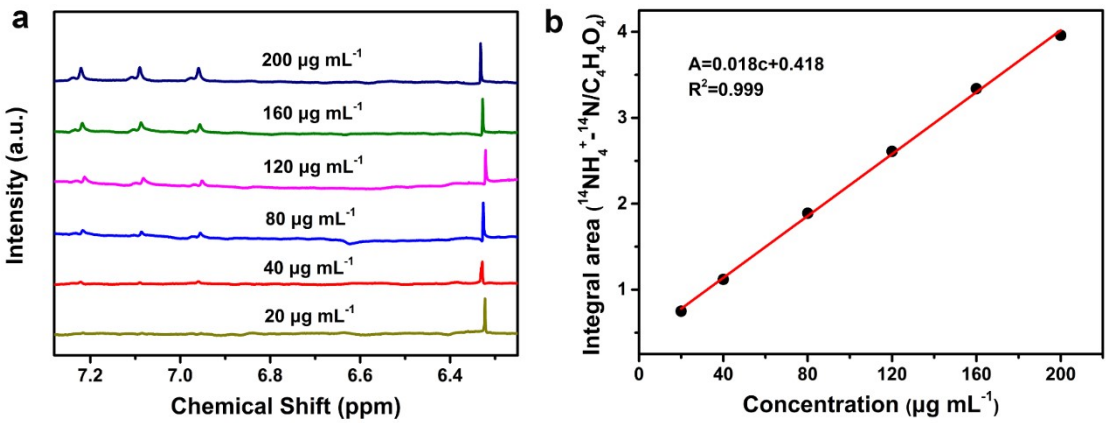

Fig. S12 (a) The ^{1}H NMR (400 MHz) spectra of $^{14}NH_4^+$ at different standard concentrations with the internal standard of $C_4H_4O_4$ and (b) corresponding calibration curve.

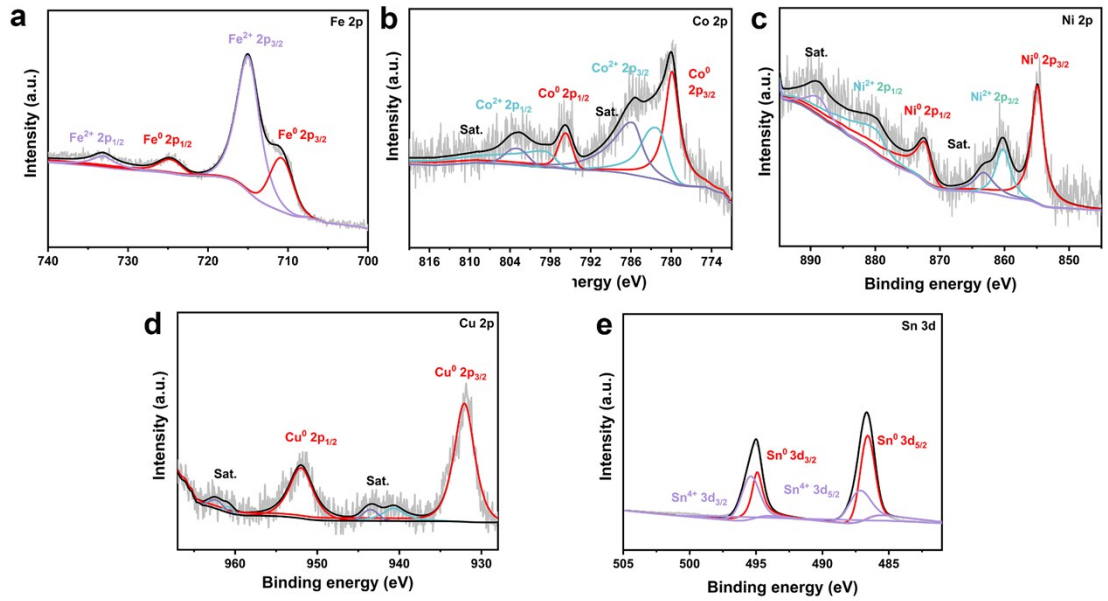

Fig. S13 XPS spectra of FeCoNiCuSn HEA after long-term electrolysis in (a) Fe 2p region, (b) Co 2p region, (c) Ni 2p region, (d) Cu 2p region and (e) Sn 3d region.

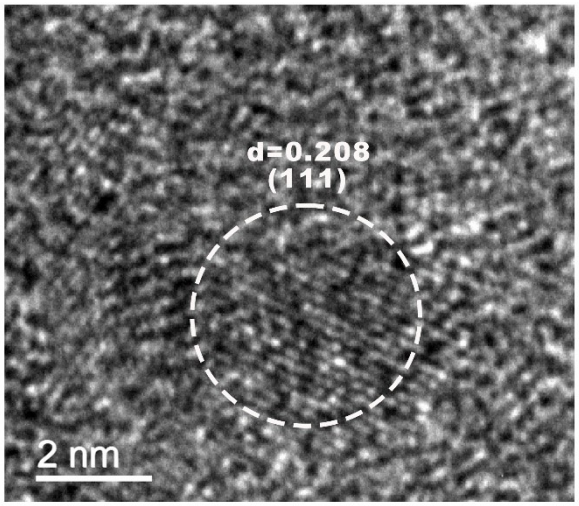

Fig. S14 TEM image of FeCoNiCuSn HEA after long-term electrolysis.

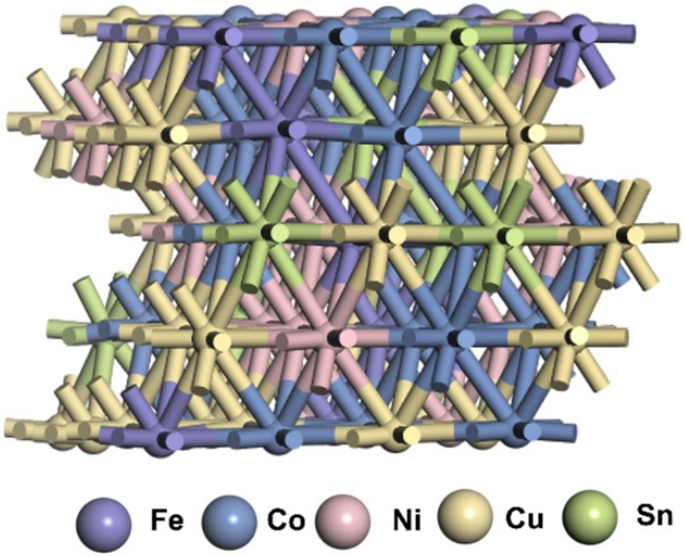

Fig. S15 The structure of FeCoNiCuSn HEA.

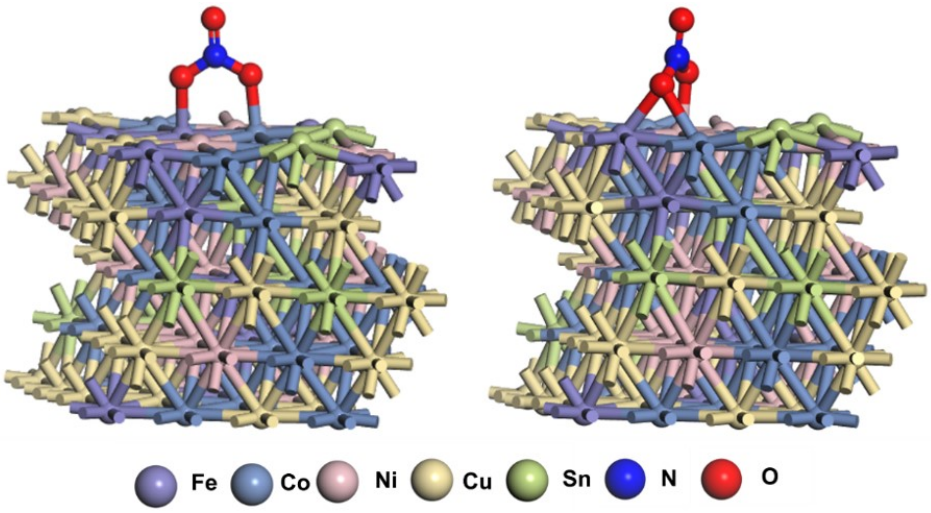

Fig. S16 Structural diagram of some sites of HEA adsorbing NO_3^-.

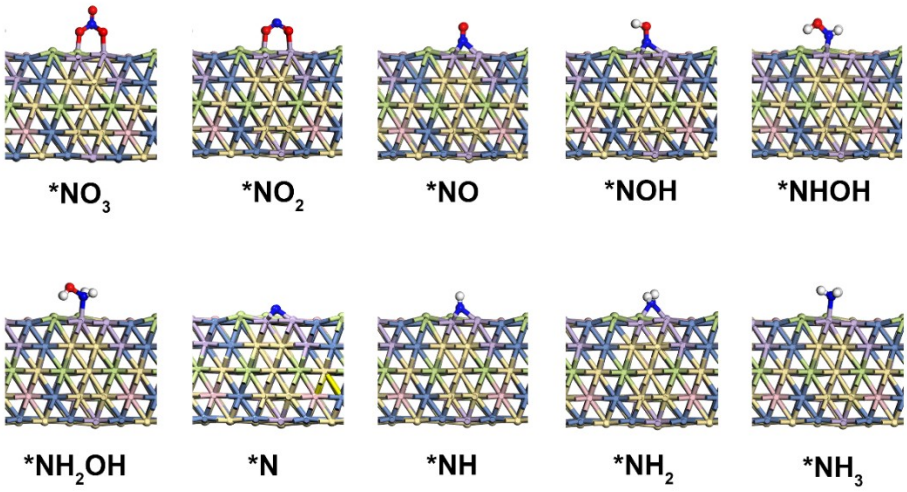

Fig. S17 Side view of various NRA intermediate structures on FeCoNiCuSn HEA surface.

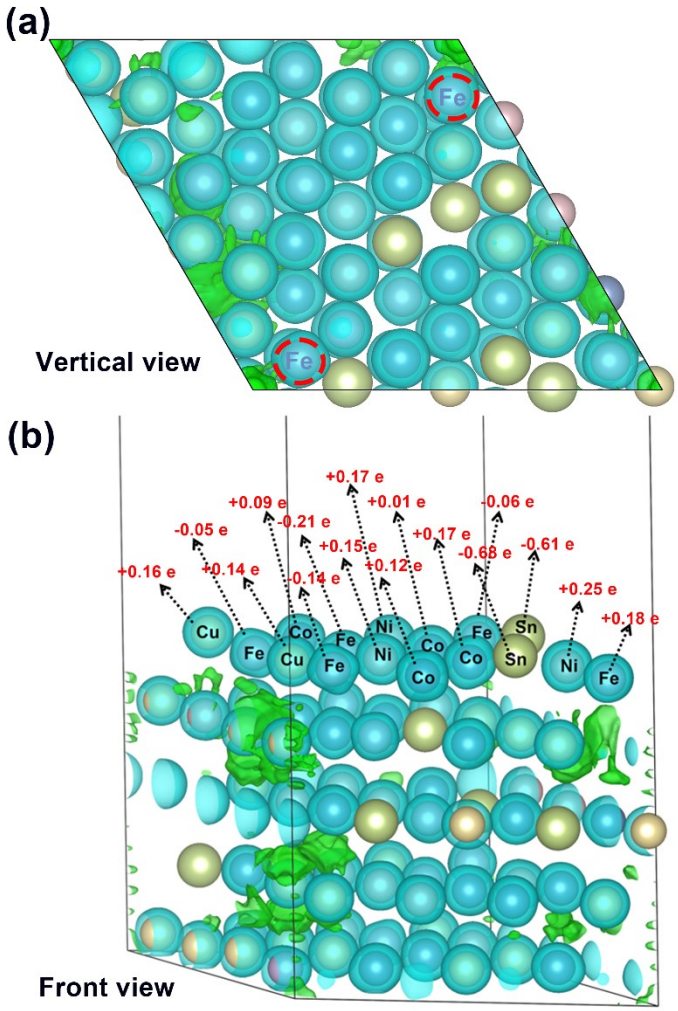

Fig. S18 Difference charge density of metal atoms before and after HEA formation (Fe-Fe site is highlighted in vertical view and the Bader charges of surface atoms are labeled with arrows).

Table S1. Elemental composition of FeCoNiCuSn samples measured by ICP-OES

Element	Element concentration in the original solution of digestion solution C_1 (mg/L)	Average element content C_x (mg/kg)	Average element content C (mg/kg)	Wt (%)	Atomic (%)
Fe	3.025	6753.212	6785.399	0.68	13.01
	3.032	6768.022			
	3.062	6834.963			
Co	4.953	11056.257	11117.627	1.11%	20.13
	4.974	11101.783			
	5.015	11194.841			
Ni	4.941	11028.506	11071.660	1.11%	20.21
	4.954	11058.741			
	4.985	11127.734			
Cu	6.034	13469.797	13580.982	1.36%	22.88
	6.093	13599.455			
	6.126	13673.695			
Sn	11.793	26322.994	26415.820	2.64%	23.77
	11.824	26392.617			
	11.886	26531.850			

Table S2. Physicochemical properties of elemental precursor salts and corresponding metals.

Precursors	Chemical reduction potential [V]	Metal	Atomic radius [Å]
$FeCl_3$	0.77, -0.44	Fe	1.26
$CoCl_2$	-0.277	Co	1.25
$NiCl_2$	-0.25	Ni	1.24
$CuCl_2$	0.34	Cu	1.28
$SnCl_2$	-0.1375	Sn	1.51

Note: source of data: Dean, John A., Lange's Handbook of Chemistry (China Science Publishing & Media Ltd.) (2003).

Table S3. Summary of the representative reports on electrocatalytic nitrate reduction to ammonia at ambient conditions.

Catalyst	System	Performance	Ref.
TiO_{2-x}	0.5 M Na_2SO_4, 50 ppm NO_3^--N	$Y(NH_3)$:630 μg h^{-1} mg^{-1} FE(NH_3): 85.0%	[9]
PTCDA/ Cu	0.1 M PBS, 500 ppm NO_3^--N	$Y(NH_3)$: 436 μg h^{-1} cm^{-2} FE(NH_3): 77%	[10]
CuCl_BEF	0.5 M Na_2SO_4, 50 ppm NO_3^--N	$Y(NH_3)$: 1820 μg h^{-1} cm^{-2} FE(NH_3): 44.7%	[11]
Cu@C	1 M KOH, 1 mM NO_3^-	$Y(NH_3)$: 469.5 μg h^{-1} cm^{-2} FE(NH_3): 72%	[12]
Cu(111) nanodisks	0.1 M KOH, 10 mM KNO3	$Y(NH_3)$: 2.1 mg h^{-1} mg_{cat}^{-1} FE(NH_3): 72%	[13]
Au/Cu SAAs	0.5 M Na_2SO_4, 100 ppm NO_3^--N	$Y(NH_3)$: 3.2 mg h^{-1} cm^{-2} FE(NH_3): 99.69%	[14]
Pd-NDs/Zr-MOF	0.1 M Na_2SO_4, 500 ppm NO_3^--N	$Y(NH_3)$: 287.31 μg h^{-1} cm^{-2} FE(NH_3): 58.1%	[15]
Cu_3P NA/CF	0.1 M PBS 0.1 M $NaNO_3$	$Y(NH_3)$: 848 μg h^{-1} cm^{-2} FE(NH_3): 62.9%	[16]
Au/C	0.5 M K_2SO_4 1 mM KNO_3	$Y(NH_3)$: 407.3 μg h^{-1} mg_{cat}^{-1} FE(NH_3): 26%	[17]
RuNi-MOF	0.1 M Na_2SO_4 50 ppm $NaNO_3$	$Y(NH_3)$: 274 μg h^{-1} mg_{cat}^{-1} FE(NH_3): 73%	[18]
Co-SACs	0.02 M Na_2SO_4 50 ppm $NaNO_3$	$Y(NH_3)$: 408 μg h^{-1} cm^{-2} FE(NH_3): 92%	[19]
Cu/Fe-TiO_2	0.5 M Na_2SO_4 50 ppm $NaNO_3$	$Y(NH_3)$: 505.7 μg h^{-1} cm^{-2} FE(NH_3): 91.2%	[20]
FeCoNiCuSn HEA	**0.1 M Na_2SO_4, 100 ppm NO_3^--N**	**$Y(NH_3)$: 883.7 μg h^{-1} cm^{-2} FE(NH_3): 94.5%**	**This work**

Table S4. Mass and percent of Fe, Co, Ni, Cu, Sn dissolved in electrolyte after electrolysis for one hour at −1.0 V vs. RHE

Element	Fe		Co		Ni		Cu		Sn	
site	E (ev)		site	E (ev)		site		E (ev)		
Mass (mg)	0.00269		0.000215		0.000508		0.000331		0.000355	
Cu1-Fe1	-447.24		Fe3_Co3		-447.75		Fe4_Fe2		-447.98	
Percent (%)	0.00898%		0.00072%		0.00169%		0.00110%		0.00118%	
Fe1_Cu2	-447.32		Co3_Sn2		-447.29		Sn2_Cu2		-446.92	
Cu2_Fe2	-447.46		Cu2_Ni1		-447.82		Sn2_Fe1		-447.32	
Co1_Fe3	-447.24		Ni1_Co4		-447.66		Ni3_Fe1		-447.41	
Fe3_Ni1	-447.70		Co4_Fe3		-447.02		Ni3_Cu2		-447.04	
Ni1_Co2_Fe2	-447.68		Fe2_Co2		-447.78		Fe5_Fe2_Cu2		-447.57	
Ni2_Co3	-447.45		Co2_Sn1		-447.21		Fe5_Fe2		-447.92	
Co3_Co4_Ni1	-447.67		Sn1_Fe5		-447.37		Fe4_Fe5		-447.92	
Co4_Sn1	-447.20		Co1_Fe1		-447.70		Ni2_Fe5_Fe4		-447.57	

Fe4_Sn2	-447.43	Ni2_Fe3	-447.44	Fe4_Fe5_Ni2	-447.57
Sn2_Ni3	-447.57	Ni2_Fe4	-447.56	Co1_Sn1	-447.331
Ni3_Fe5	-447.5	Fe3_Cu2	-447.32	Co1_Co2	-447.50
Cu1_Co1	-447.28	Co3_Ni1	-447.71	Cu1_Co2	-447.34
Co1_Ni2	-447.41	Sn2_Co4	-447.21	Cu1_Fe2	-447.48
Fe4_Co3	-447.79	Co4_Co2	-447.51	Fe4_Co3_Sn2	-447.18
Fe1_Fe3	-447.75	Ni3_Sn2	-447.01		

Table S5. The suitable adsorption site and the enthalpy of formation.

Table S6. The correction of electronic energies (E), zero-point energies (ZPE) and entropy (TS) of adsorption species on different catalysts' surfaces (in eV). All the slab atoms were fixed during the vibrational analyses. (T = 298.15 K)

	E	ZPE	TS
*NO_3	-472.93	0.40	0.25
*NO_2	-467.51	0.26	0.19
*NO	-462.27	0.17	0.11
*NOH	-465.74	0.46	0.15
*NHOH	-468.89	0.76	0.19
*NH_2OH	-472.44	1.11	0.22
*N	-456.11	0.08	0.02
*NH	-460.32	0.37	0.04

$*NH_2$	-460.69	0.67	0.09
$*NH_3$	-467.21	1.00	0.17

References

[1] G. Kresse and J. Hafner, Ab initio molecular dynamics for open-shell transition metals, *Phys. Rev. B*, 1993, **48**, 13115-13118.

[2] G. Kresse and J. Furthmuller, Efficient iterative schemes for ab initio total-energy calculations using a plane-wave basis set, *Phys. Rev. B*, 1996, **54**, 11169-11185.

[3] P. E. Blochl, Projector augmented-wave method, *Phys. Rev. B*, 1994, **50**, 17953-17979.

[4] J. P. Perdew, K. Burke and M. Ernzerhof, Generalized gradient approximation made simple, *Phys. Rev. Lett.*, 1996, **77**, 3865-3868.

[5] S. Grimme, J. Antony, S. Ehrlich and H. Krieg, A consistent and accurate ab initio parametrization of density functional dispersion correction (DFT-D) for the 94 elements H-Pu, *J. Chem. Phys.*, 2010, **132**, 154104.

[6] A. van de Walle, Multicomponent multisublattice alloys, nonconfigurational entropy and other additions to the Alloy Theoretic Automated Toolkit, *Calphad.,* 2009, **33**, 266–278.

[7] A. van de Walle, P. Tiwary, M. de Jong, D. L. Olmsted, M. Asta, A. Dick, D. Shin, Y. Wang, L. Q. Chen and Z. K. Liu, Efficient stochastic generation of special quasirandom structures, *Calphad.*, 2013, **42**, 13-18.

[8] J. X. Liu, D. Richards, N. Singh and B. R. Goldsmith, Activity and selectivity trends in electrocatalytic eitrate reduction on transition metals, *ACS Catal.*, 2019, **9**, 7052−7064.

[9] R. Jia, Y. Wang, C. Wang, Y. Ling, Y. Yu and B. Zhang, Electroreduction to ammonium by constructing oxygen vacancies in TiO_2, *ACS Catal.*, 2020, **10**, 3533-3540.

[10] G. F. Chen, Y. Yuan, H. Jiang, S. Y. Ren, L. X. Ding, L. Ma, T. Wu, J. Lu and H. Wang, Electrochemical reduction of nitrate to ammonia via direct eight-electron transfer using a copper–molecular solid catalyst, *Nat. Energy*, 2020, **5**, 605-613.

[11] W. J. Sun, H. Q. Ji, L. X. Li, H. Y. Zhang, Z. K. Wang, J. H. He and J. M. Lu, Built-in electric field triggered interfacial accumulation effect for efficient nitrate removal at ultra-low concentration and electroreduction to ammonia, *Angew. Chem. Int. Edit.*, 2021, **60**, 22933-22939.

[12] Z. Song, Y. Liu, Y. Zhong, Q. Guo, J. Zeng and Z. Geng, Efficient electroreduction of nitrate into ammonia at ultralow concentrations via an enrichment effect, *Adv. Mater.*, 2022, **34**,

2204306.

[13] K. Wu, C. Sun, Z. Wang, Q. Song, X. Bai, X. Yu, Q. Li, X. Wang, H. Zhang, J. Zhang, X. Tong, Y. Liang, A. Khosla and Z. Zhao, Surface reconstruction on uniform Cu nanodisks boosted electrochemical nitrate reduction to ammonia, *ACS Materials Lett.*, 2022, 650-656.

[14] H. Yin, Y. Peng and J. Li, Electrocatalytic reduction of nitrate to ammonia via a Au/Cu single atom alloy catalyst, *Environ. Sci. Technol.*, 2023, **57**, 3134-44.

[15] M. Jiang, J. Su, X. Song, P. Zhang, M. Zhu, L. Qin, Z. Tie, J. Zuo and Z. Jin, Interfacial reduction nucleation of noble metal nanodots on redox-active metal-organic frameworks for high-efficiency electrocatalytic conversion of nitrate to ammonia, *Nano Lett.*, 2022, **22**, 2529-37.

[16] J. Liang, B. Deng, Q. Liu, G. Wen, Q. Liu, T. Li, Y. Luo, A. A. Alshehri, K. A. Alzahrani, D. Ma and X. Sun, High-efficiency electrochemical nitrite reduction to ammonium using a Cu_3P nanowire array under ambient conditions, *Green Chem.*, 2021, **23**, 5487-5493.

[17] J. Choi, H. Du, C. K. Nguyen, B. H. R. Suryanto, A. N. Simonov and D. R. MacFarlane, Electroreduction of nitrates, nitrites, and gaseous nitrogen oxides: a potential source of ammonia in dinitrogen reduction studies, *ACS Energy Lett.*, 2020, **5**, 2095-2097.

[18] J. Qin, K. Wu, L. Chen, X. Wang, Q. Zhao, B. Liu and Z. Ye, Achieving high selectivity for nitrate electrochemical reduction to ammonia over MOF-supported Ru_xO_y clusters, *J. Mater. Chem. A*, 2022, **10**, 3963-3969.

[19] J. Li, M. Li, N.An and X. Liu, Boosted ammonium production by single cobalt atom catalysts with high Faradic efficiencies, *P. Natl. A. Sci.*, 2022, **119**, e2123450119.

[20] X. Yang, R. Wang, S. Wang, C. Song, S. Lu, L. Fang, F. Yin and H. Liu, Sequential active-site switches in integrated Cu/Fe-TiO_2 for efficient electroreduction from nitrate into ammonia, *Appl. Catal. B: Environ.*, 2023, **325**, 122360.